



HAL
open science

A Comparison of Circumgalactic MgII Absorption between the TNG50 Simulation and the MEGAFLOW Survey

Daniel Defelippis, Nicolas F. Bouché, Shy Genel, Greg L. Bryan, Dylan
Nelson, Federico Marinacci, Lars Hernquist

► **To cite this version:**

Daniel Defelippis, Nicolas F. Bouché, Shy Genel, Greg L. Bryan, Dylan Nelson, et al.. A Comparison of Circumgalactic MgII Absorption between the TNG50 Simulation and the MEGAFLOW Survey. The Astrophysical Journal, 2021, 10.3847/1538-4357/ac2cbf. hal-03431345

HAL Id: hal-03431345

<https://hal.science/hal-03431345>

Submitted on 26 Nov 2021

HAL is a multi-disciplinary open access archive for the deposit and dissemination of scientific research documents, whether they are published or not. The documents may come from teaching and research institutions in France or abroad, or from public or private research centers.

L'archive ouverte pluridisciplinaire **HAL**, est destinée au dépôt et à la diffusion de documents scientifiques de niveau recherche, publiés ou non, émanant des établissements d'enseignement et de recherche français ou étrangers, des laboratoires publics ou privés.

A Comparison of Circumgalactic MgII Absorption between the TNG50 Simulation and the MEGAFLOW Survey

DANIEL DEFELIPPIS ¹, NICOLAS BOUCHÉ ², SHY GENEL ^{3,4}, GREG L. BRYAN,^{1,3} DYLAN NELSON,⁵
FEDERICO MARINACCI,⁶ AND LARS HERNQUIST⁷

¹*Department of Astronomy, Columbia University, 550 West 120th Street, New York, NY 10027, USA*

²*Univ Lyon, Univ Lyon1, Ens de Lyon, CNRS, Centre de Recherche Astrophysique de Lyon UMR5574, F-69230 Saint-Genis-Laval, France*

³*Center for Computational Astrophysics, Flatiron Institute, 162 Fifth Avenue, New York, NY 10010, USA*

⁴*Columbia Astrophysics Laboratory, Columbia University, 550 West 120th Street, New York, NY 10027, USA*

⁵*Universität Heidelberg, Zentrum für Astronomie, Institut für theoretische Astrophysik, Albert-Ueberle-Str. 2, 69120 Heidelberg, Germany*

⁶*Department of Physics and Astronomy, University of Bologna, Via Gobetti 93/2, I-40129, Bologna, Italy*

⁷*Harvard-Smithsonian Center for Astrophysics, 60 Garden Street, Cambridge, MA 02138, USA*

Submitted to ApJ

ABSTRACT

The region surrounding galaxies, often called the circumgalactic medium (CGM), **contains** information on gas flows around galaxies, such as accretion and **supernova-driven winds**. Recent absorption line studies of the CGM have revealed a complicated kinematic structure, but due to the geometry **and nature** of single absorption sightlines, they cannot **constrain these processes unambiguously**. Here, we use the high-resolution TNG50 cosmological magneto-hydrodynamical simulation to study the properties and kinematics of the CGM around star-forming galaxies in $10^{11.5} - 10^{12} M_{\odot}$ halos at $z \simeq 1$ using mock MgII absorption lines. **We post-process the TNG50 simulations to account for the ionization properties of the CGM including both collisional and photoionization in the presence of a UV + X-ray background.** Here, we focus on the low-ionization line MgII, and find that the MgII gas is a **very good tracer of the cool CGM component, which is also accreting** inwards at an inflow velocity of $\sim 50 \text{ km s}^{-1}$. For sightlines aligned with the galaxy major-axis, we find that MgII absorption lines are kinematically shifted due to the cold CGM's significant co-rotation at speeds up to 50% of the virial velocity for impact parameters up to 60 kpc. **We compare mock MgII spectra to MgII observations from the MusE GAs FLOW and Wind (MEGAFLOW) survey of strong MgII absorbers ($EW_0^{2796\text{\AA}} > 0.5 \text{ \AA}$).** **We find that eventhough sight-lines are probing a very small fraction of the MgII halo, the mock spectra tend to reflect the diversity of observed kinematics and equivalent widths.** After matching the EW selection, we find that the properties of the mock MgII spectra are in good agreement with those from MEGAFLOW in terms of shape, equivalent widths (EW) and kinematics. MgII absorption in higher-mass halos is stronger and broader than in lower-mass halos at $z = 1$ but has qualitatively similar kinematics.

Keywords: galaxies: formation – galaxies: kinematics and dynamics – galaxies: structure – hydrodynamics – methods: numerical

1. INTRODUCTION

The accretion of gas onto disk galaxies is a fundamental part of galaxy formation and evolution, as gas within disks is continually used to form stars and must therefore be regularly replenished (e.g., Putman 2017). All such gas, whether pristine from cosmological inflows or recycled gas in the process of reaccreting, must pass through

the local environment surrounding galaxies, often called the circumgalactic medium (CGM). The CGM might contain a substantial amount of angular momentum as shown by many studies of galaxy simulations (e.g. Stewart et al. 2011; Danovich et al. 2015; DeFelippis et al. 2020). As the gas accretes onto the galaxy, the angular momentum will flow inwards too, meaning the CGM is a source not just of the mass of the disk, but its angular momentum as well.

Not all gas surrounding galaxies is inflowing though: the CGM also contains outflowing gas ejected from the galaxy by feedback from supernovae and active galactic nuclei (AGN), which is capable of affecting the way in which CGM gas eventually joins the galaxy (DeFelippis et al. 2017). All of these physical processes occur concurrently and result in a multiphase environment shown in observations to have **complex** kinematics (see Tumlinson et al. 2017, and references therein).

A large number of recent observations of the CGM have been accomplished through absorption line studies of background quasars through dedicated surveys. For instance, some surveys are constructed by cross-correlating quasar absorption lines with spectroscopic redshift surveys such as the Keck Baryonic Structure Survey (KBSS: Rudie et al. 2012; Turner et al. 2014) or with photometric surveys like SDSS (Lan & Mo 2018; Lan 2020). Other CGM surveys attempt to either match individual absorption lines to known galaxies (i.e. are “galaxy-selected”), like the COS-Halos (e.g. Tumlinson et al. 2011; Werk et al. 2013; Burchett et al. 2019) and the low-redshift Keck surveys **conducted at Keck Observatory** (Ho et al. 2017; Martin et al. 2019), or match galaxies near known absorbers (i.e. “absorber-selected”) such as the MusE GAS FLOW and Wind survey (MEGAFLOW: Schroetter et al. 2016, 2019, 2021; Wendt et al. 2021; Zabl et al. 2019, 2020, 2021).

The MgII ion has been a focus of many recent surveys including the MgII Absorber-Galaxy Catalog (MAGICAT: e.g. Nielsen et al. 2013, 2015), the MUSE Analysis of Gas around Galaxies Survey (MAGG: Dutta et al. 2020), ~~it has inspired subsequent analysis of surveys like the PRISM Multi-object Survey (PRIMUS: Coil et al. 2011; Rubin et al. 2018)~~ and the aforementioned MEGAFLOW survey. These studies belong to a long history of MgII $\lambda 2796$ absorption line surveys (e.g. Bergeron & Boissé 1991; Bergeron et al. 1992; Steidel & Sargent 1992), which unveiled the first galaxy-absorber pairs at intermediate redshifts. **Though not the focus of this paper, MgII has also been seen in emission in extended structures around the galaxy and in the CGM (e.g. Rubin**

et al. 2011; Rickards Vaught et al. 2019; Rupke et al. 2019; Burchett et al. 2020; Zabl et al. 2021).

Along with this wealth of MgII observations, researchers in recent years have found MgII kinematics to be correlated over large spatial scales. In particular, both Bordoloi et al. (2011) and Bouché et al. (2012) found a strong dependence of MgII absorption with azimuthal angle: specifically, more absorption near $\phi = 0^\circ$ and 90° and a lack of absorption near 45° . This type of absorption distribution is generally interpreted as bipolar outflows along the minor axis and inflows along the major axis. In this context, both galaxy-selected (e.g. Ho et al. 2017; Martin et al. 2019) and absorption-selected MgII studies (e.g. Bouché et al. 2013, 2016; Zabl et al. 2019) have given support to the interpretation of accretion of gas from the CGM onto the galaxy. **These MgII studies show that when sightlines are located near the major axis of the galaxy there are clear signatures of corotating cold gas with respect to the galaxy kinematics.**

However, despite such extensive observational data, developing a general understanding of cold gas in the CGM from the MgII line alone remains difficult due to the limited spatial information provided by **the observational technique (though IFU mapping of lensed arcs in e.g. Lopez et al. 2020 and Mortensen et al. 2020 can improve this in the future)**, as well as the fact that MgII gas may not be representative of the entire cold phase of the CGM. To study more physically fundamental properties of the CGM, it is therefore necessary to turn to galaxy simulations.

In cosmological simulations, the CGM has been notoriously difficult to model accurately due to the need to resolve very small structures (see Hummels et al. 2019; Peebles et al. 2019; Suresh et al. 2019; Corlies et al. 2020). Nonetheless, the CGM has been shown to preferentially align with and rotate in the same direction of the galaxy, especially near the galaxy’s major axis (Stewart et al. 2013, 2017; Ho et al. 2019; DeFelippis et al. 2020), which is qualitatively consistent with observations in the same spatial region of the CGM (e.g. Zabl et al. 2019). However, this general qualitative agreement between simulations and observations is difficult to put on firm grounds quantitatively due to differences in **how gas phases are generally measured in simulations using density and temperature cuts vs. how they are understood from observations with ionic tracers like MgII. NB:This is vague to me. Perhaps:[...] is difficult to put on firm grounds quantitatively due to inherent differences between observations and simulations.**

In this paper, we analyze a set of halos from the TNG50 simulation (Nelson et al. 2019; Pillepich et al. 2019) using the TRIDENT tool (Hummels et al. 2017) to model the ionization state of the CGM and then perform a quantitative comparison of the kinematics of the cool ($T \lesssim 3 \times 10^4$ K) CGM traced by MgII to major-axis sightlines from the MEGAFLOW survey (Zabl et al. 2019) while attempting to match the observational selection criteria as described in Section 2. We note that our **comparison to MEGAFLOW galaxies with stellar masses** $M_* \sim 10^{10} M_\odot$ is complementary to that of Nelson et al. (2020) who study the origins of cold CGM gas of very massive galaxies ($M_* > 10^{11} M_\odot$).

The paper is organized as follows. In Section 2, we describe the TNG50 simulation and MEGAFLOW sample used in the comparison, and we outline the analysis pipeline used to generate mock observations. In Section 3, we describe our main results, first by comparing the simulated and real observations, then by analyzing the features of the simulation that give rise to the properties of the mock observations. In Section 4, we discuss the implications of our results for the role of the CGM in galaxy formation, and we summarize our findings in Section 5.

2. METHODS

2.1. Simulations

We utilize the TNG50 simulation (Nelson et al. 2019; Pillepich et al. 2019), the highest resolution version of the IllustrisTNG simulation suite (Marinacci et al. 2018; Naiman et al. 2018; Nelson et al. 2018; Pillepich et al. 2018; Springel et al. 2018). TNG50 evolves a periodic $\approx (52 \text{ Mpc})^3$ box from cosmological initial conditions to $z = 0$ with the moving-mesh code AREPO (Springel 2010; Weinberger et al. 2019). It has a baryonic mass resolution of $\sim 8.5 \times 10^4 M_\odot$ per cell, which is a factor of ≈ 16 better than the resolution of TNG100. We discuss the effect of simulation resolution on our results later in Section 3.

2.2. Observational Data

~~NB:We will compare our mock observations to the Muse GAs FLOW and Wind (MEGAFLOW) survey.~~ The MEGAFLOW survey (Bouché et al., in prep.) consists of a sample of 79 MgII $\lambda\lambda 2796, 2803$ absorbers in 22 quasar lines-of-sight observed with the Multi-Unit Spectrograph Explorer (MUSE: Bacon et al. 2006). The quasars were selected to have at least three MgII absorbers from the Zhu & Ménard (2013) SDSS catalog in the redshift range $0.4 < z < 1.4$ such that the [OII] $\lambda\lambda 3727, 3729$ galaxy emission lines fell within the MUSE wavelength range (4800 – 9300 Å). A threshold on the

rest-frame equivalent width of $\sim 0.5 - 0.8$ Å was also imposed on each absorber.

For this paper, we focus on a preliminary subset of the MEGAFLOW sample of MgII absorber-galaxy pairs whose quasar location is positioned within 35° of the major axis of the host galaxy (Zabl et al. 2019). This subset, consisting of nine absorber-galaxy pairs **with redshifts** $0.5 < z < 1.4$ and **Zabl et al. (2019) found that the MgII gas show** a strong preference for corotation with their corresponding host galaxies. The MgII absorbers themselves have a mean impact parameter (b) of ≈ 34 kpc while ranging from 17 – 65 kpc from the galaxy.

The galaxies in Zabl et al. (2019) are both fairly isolated by having at most one companion within 100 kpc and star-forming with [OII] fluxes $f_{\text{OII}} > 4 \times 10^{-17} \text{ erg s}^{-1} \text{ cm}^{-2}$, i.e. ~~NB:All galaxies in this sample~~ have star-formation rates $\gtrsim 1 M_\odot \text{ yr}^{-1}$. The galaxies ~~NB:in this sample~~ have a mean stellar mass $M_* \approx 10^{10} M_\odot$ and a mean halo mass of $M_{\text{vir}} \approx 7 \times 10^{11} M_\odot$, where M_{vir} is defined from Bryan & Norman (1998) and inferred from the measured rotation velocity of the absorber (for further details see Zabl et al. 2019). ~~NB:Here you quote the mean, but we should quote the range, no? since you use the range in the next section?/ They are from 11.4 to 11.8. and 11.5 to 12 if scaled to $z = 0.5$.~~

2.3. Sample selection and forward-modeling

~~NB:I reorganized a bit.~~ Figure 1 shows the central galaxies' **instantaneous** star formation rates (SFR) and stellar masses of **all** TNG50 halos in and around the mass range of interest.

Since we aim to compare the MgII absorption properties of mock line-of-sight observations through TNG50 halos to those of major-axis sight-lines of the MEGAFLOW survey, we first select a sample of simulated halos at $z = 1$ in the mass range $10^{11.5} M_\odot < M_{\text{halo}} < 10^{12} M_\odot$ **using the Bryan & Norman (1998) definition for M_{halo}** , which results in a sample of 495 halos. **In the remainder of this paper, we will refer to this sub-sample as the ‘fiducial’ sample.**

The chosen redshift is typical for the Zabl et al. (2019) sample and the halo mass range covers the mean inferred virial masses of their host galaxies. ~~NB:Currently, we didn't show the mass range?~~ Nearly all of the halos in our fiducial ~~NB:Fiducial is not defined?~~ mass range **host central galaxies with SFR $\gtrsim 1 M_\odot \text{ yr}^{-1}$** and stellar masses of $\sim 10^{10} M_\odot$, which is consistent with MEGAFLOW sub-sample as described in Section 2.2.

For each halo, we adjust all velocities to be in the center-of-mass frame of the stars in the central galaxy,

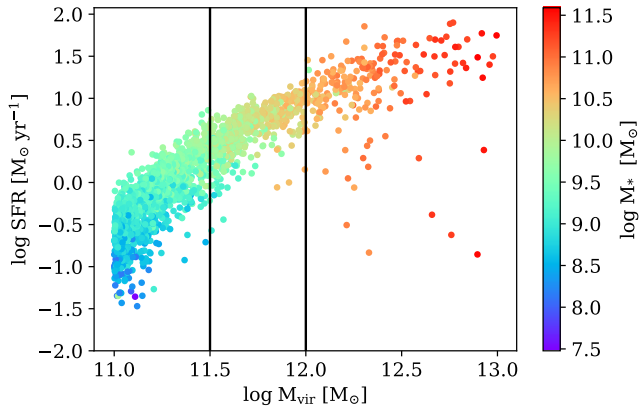


Figure 1. Star formation rate of the central galaxy vs. halo mass for all TNG50 halos between $10^{11} M_{\odot}$ to $10^{13} M_{\odot}$ at $z = 1$. Each point is colored by the stellar mass of the halo’s central galaxy. Two vertical lines demarcate the halo mass range of the fiducial sample.

and we rotate it so that the stellar specific angular momentum of the central galaxy points in the $+z$ -direction (the x and y directions are both arbitrary). With this geometry we then define a sightline in the $x-z$ plane by the impact parameter b , the azimuthal angle α , and the inclination angle i , where b is the projected distance from the center of the galaxy in the $y-z$ plane (i.e. “sky”-plane), α is the angle above the rotational plane of the galaxy, and i is the angle of the sightline with respect to the sky-plane. In this setup, edge-on and face-on views have $i = 90^{\circ}$ and $i = 0^{\circ}$ respectively (see Figure 1 of Zabl et al. 2019, for a sketch of the geometry described here). In order to mimic the observations of Zabl et al. (2019), we select sightlines through each halo at values of b ranging from 15 kpc to 60 kpc, $\alpha = 5^{\circ}$ and 25° , and at $i = 60^{\circ}$, representing the average inclination angle of a random sightline.

NB: This paragraph would need more physical description. What physical processes are included? not included? what UV background? Cfr abstract In order to generate observations of our TNG50 sample, we use the TRIDENT package (Hummels et al. 2017), which calculates ionization parameters for outputs of galaxy simulations using properties of the simulated gas cells and CLOUDY (Ferland et al. 2013) ionization tables. These tables take as input the gas temperature, density, metallicity, and cosmological redshift of each gas cell and provide ionization fractions and number densities of desired ions. **We make use of the current development**

version of TRIDENT¹ (v1.3), which itself depends on the current development version of YT² (v4.0). **NB:** Do we need this at all??: We choose these software versions because rather than generating a new grid to deposit the Arepo gas cells into (as the stable versions do), they treat the gas cells as particles that are individually smoothed, thus removing grid artifacts that would be otherwise present.

Since our focus is on the MgII $\lambda 2796$ line, we show In Figure 2 we show a temperature-density phase diagram of the gas in one of the TNG50 halos from our sample, colored by the MgII mass probability density. From this plot, it is clear that MgII is mostly formed from the coldest ($\lesssim 10^{4.5}$ K) and densest ($\gtrsim 0.01 \text{ cm}^{-3}$) gas in the halo, though some MgII mass exists at a larger range of temperatures and densities. However, contours showing the total gas mass demonstrate that despite this large range in temperature and density, essentially none of the diffuse “hot” phase, comparable in mass to the cold phase, contributes to MgII absorption. We also note here that for this analysis we are excluding star-forming gas defined from its an effective equation of state from Springel & Hernquist (2003) and are therefore not analogous to the physical properties of non-star-forming gas. Properly modeling the physical properties of the star-forming gas (see Ramos Padilla et al. 2020, for an example of this technique) introduces a level of complexity not necessary for this analysis: we find that our results are not affected by the exclusion of this gas since our sightlines through the CGM rarely intersect any star-forming gas cells as most of them are within the galactic disk.

We make two adjustments to TRIDENT’s default settings, both to achieve greater self-consistency with TNG50. First, we use the elemental abundance of magnesium in each gas cell tracked by TNG50 rather than assuming a constant solar abundance throughout the halo. We also use a set of ion tables created with a Faucher-Giguère et al. (2009) UV-background that includes self-shielding, as this was the background radiation model used to evolve the TNG50 simulation. We note, however, that our results are not particularly sensitive to either of these alterations.

3. RESULTS

¹ trident-project.org

² yt-project.org

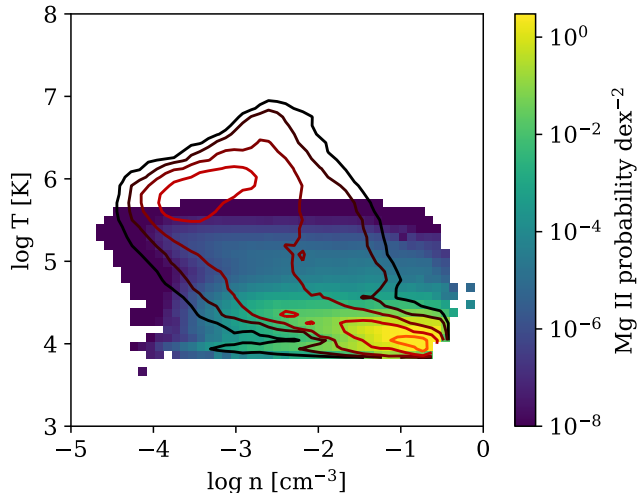


Figure 2. Temperature-number density phase diagram of a single TNG50 halo at $z = 1$, colored by the MgII mass probability density per dex². Contours show the distribution of all gas mass in the halo.

We first present in Section 3.1 the results of directly comparing the MgII properties of TNG50 and MEGAFLOW using the analysis described in Section 2. Then, we further analyze the 3D kinematic properties of the MgII bearing gas from TNG50 in Section 3.2 and consider evolution of MgII absorption properties with halo mass and simulation resolution in Section 3.3.

3.1. Comparing TNG50 to MEGAFLOW

In Figure 3, we show MgII column density maps of a selection of TNG50 halos drawn from our fiducial halo mass bin at $z = 1$. **The halos are aligned so that the angular momentum vector of the stars in the central galaxy points along the vertical axis: thus, the view is edge-on.** The strongest MgII columns are found within and very close to the galaxy, demarcated by a red circle with a radius of twice the galaxy’s stellar half-mass radius (the same definition used in DeFelippis et al. 2020). Beyond the galaxy, the amount and morphology of the MgII gas varies greatly, but it consistently appears to both surround the galactic disk and be very clumpy, though it is not spherically symmetric. The highest MgII columns generally appear in the plane of rotation, but strong columns can occur above and below the disk as well, such as in halo 265 (the bottom left panel of Figure 3). High MgII columns are much less common in the outer halo ($r \gtrsim 50$ kpc), but the presence of satellite galaxies can populate that region with MgII gas, shown most clearly in halo 340 (the bottom right panel).

Within our fiducial halo mass bin, it is evident that the distribution of MgII varies drastically, presumably due to different halo formation histories. Sightlines through different halos will therefore likely produce different absorption profiles even for sightlines with identical geometries. This highlights the necessity of calculating population averages of MgII properties from TNG50 to compare to MEGAFLOW.

We begin such a comparison with Figure 4, which shows the average strength of MgII absorption, represented as the rest-frame equivalent width (EW_0) as a function of impact parameter (b) for our fiducial sample. In this plot, we make an important distinction between the entire fiducial sample, shown in black, and the subset of “strong absorbers” in red. We define strong absorbers as sightlines through a halo that produce an absorption spectrum with $EW_0 > 0.5 \text{ \AA}$ (the same as in Zabl et al. 2019). It is this “absorber-selected” subset of the fiducial sample that is most directly comparable to MEGAFLOW.

At all impact parameters, the **average rest-frame EW of the ‘all absorbers’ sample from TNG50 is smaller than those of MEGAFLOW, as expected given the selection function. The difference ranges** from a factor of only ≈ 3 at $b \leq 20$ kpc to a factor of ≈ 30 at 60 kpc. If, instead, we compare the average EW_0 of the strong absorber subset ($EW_0 > 0.5 \text{ \AA}$) from TNG50, which is **the appropriate comparison to make**, we find the mean shown in red. This is much more similar to the values from MEGAFLOW, especially for $b \geq 40$ kpc, but it is still about a factor of ≈ 2 lower than the observed values at $b \leq 20$ kpc. Sightlines at $\alpha = 5^\circ$ (solid) and $\alpha = 25^\circ$ (dotted) produce essentially identical equivalent widths over both the entire fiducial sample and the subset of strong absorbers.

The blue lines in Figure 4 show the fraction of all sightlines that host strong absorbers as a function of impact parameter. At sightlines very close to the galaxy ($b = 15$ kpc), strong absorbers are common and in fact represent a majority of all halos. However, by $b = 20$ kpc the strong absorber fraction drops below 50%, and at the largest impact parameters shown, the fraction is only $\approx 1\%$. Strong absorbers are slightly more common at $\alpha = 5^\circ$ compared to $\alpha = 25^\circ$, which can be understood by noting that the sightlines with smaller α pass through the **disk midplane** closer to the galaxy’s center, where gas is generally denser. However, this difference in strong absorber fraction does not affect the measured equivalent widths, indicating that the TNG50 halos’ agreement with MEGAFLOW for sightlines near

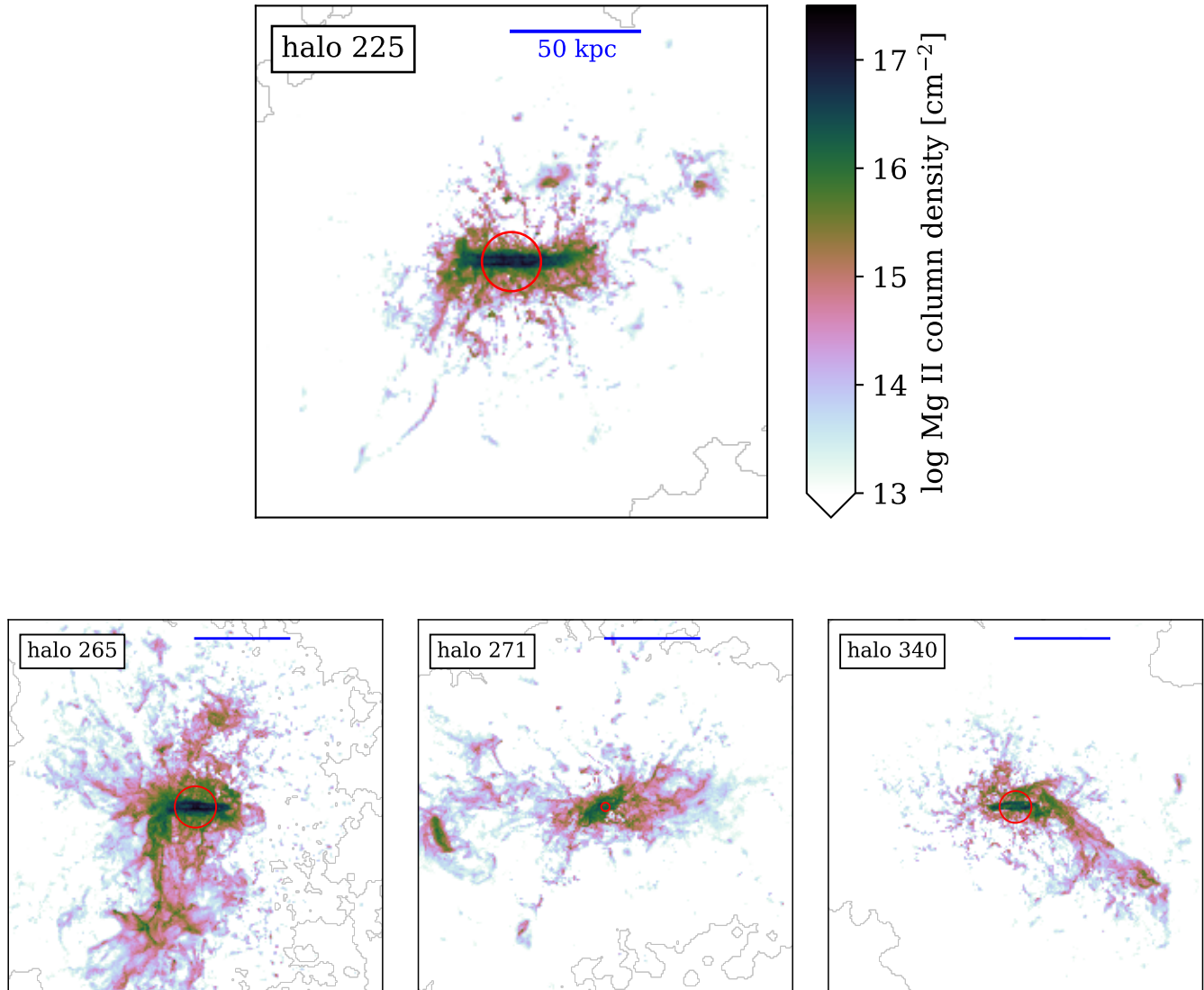


Figure 3. Mg II column density maps of four TNG50 halos from the fiducial halo mass bin of $10^{11.5} M_{\odot} < M_{\text{halo}} < 10^{12} M_{\odot}$ at $z = 1$, aligned so the angular momentum vector of the stars in the **central** galaxy points along the vertical axis (**i.e. edge-on**). The lower limit of the colorbar is chosen to approximate observational detection limits. The red circle in each panel is centered on the galaxy and has a radius of twice the galaxy’s stellar half-mass radius, **and the blue scale-bar shows a distance of 50 kpc on the maps**. The complexity and diversity of Mg II structure in the CGM of similar-mass halos is evident even in this small sample.

the galaxies’ major axes is not subject to the precise choice of sightlines.

Having established the degree of consistency of Mg II equivalent widths, we now examine kinematic signatures of Mg II along sightlines in TNG50 and compare them to MEGAFLOW. In Figure 5, we explicitly draw the connection between the Mg II gas cells that contribute to the column densities seen in Figure 3 and the velocity spectrum created from a subset of those cells that intersect a sightline through the halo. In each row, we show

two orientations of one of the four halos from Figure 3 overlaid with a sightline with $b = 30$ kpc, $\alpha = 5^{\circ}$, and $i = 60^{\circ}$, and the Mg II velocity spectrum generated from that sightline. From these few examples it is clear that the gas producing the Mg II absorption is generally not distributed uniformly along any sightline: it is usually concentrated in discrete clumps in regions of the sightline nearest to the galaxy. This is seen clearly in rows one, two, and four, where the majority of gas cells have positive line-of-sight velocities (*i.e.* corotating with the

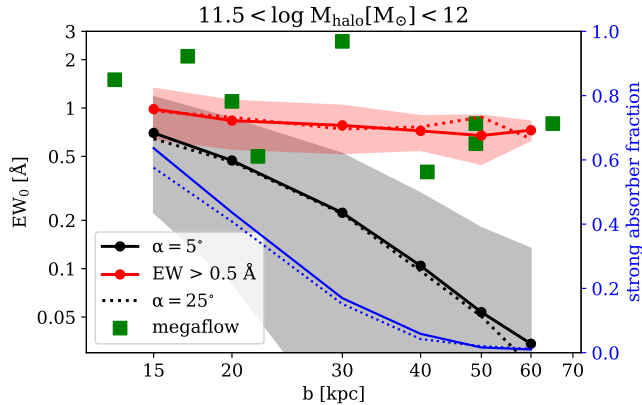


Figure 4. Mean MgII equivalent widths of halos in our fiducial sample vs. the impact parameter of sightlines through those halos. Black and red lines and corresponding shaded regions show mean and $\pm 1\sigma$ scatter of all halos and the subset of strong absorbers ($EW_0 > 0.5 \text{ \AA}$) respectively. Sightlines at a constant azimuth angle of $\alpha = 5^\circ$ and 25° are shown with solid and dotted lines respectively. Observations of individual systems from MEGAFLOW (Zabl et al. 2019) are shown as green squares. The fraction of strong absorbers as a function of impact parameter (blue) is shown with the right vertical axis.

galaxy) and produce distinct kinematic components in the spectrum that are often saturated.

It is also notable that by comparing the spectra alone it is possible to distinguish morphological differences in the MgII distribution between halos. The first two halos, for example, have a prominent MgII disk that both spectra reveal to be primarily corotating. The halo in row three, however, does not have such a clear disk, and the spectrum is instead composed of a cluster of counter-rotating gas cells significantly above the plane of the galaxy. The halo in row four has a spectrum with substantial co-rotating and counter-rotating components, which imply MgII structure in between the ordered halos (rows one and two) and disordered ones (row three). With this small sample, we have demonstrated that the velocity spectrum, despite being composed of a very small fraction of all of the MgII gas, is capable of reflecting both NB:both what? the potential diversity of MgII gas kinematics in halos of similar mass, but is also fairly consistent between halos with similar morphologies.

From these results, we now compare a stack spectra from the fiducial sample to the stacked spectra presented in Zabl et al. (2019) NB:; confident that the kinematics found in the TNG50 halos are well represented. Later in the paper, we consider whether the MgII gas

reflects the kinematics of other components of the CGM. NB:Not sure what the previous sentence adds? Figure 6 shows a stacked spectra for the entire TNG50 fiducial sample, TNG50 strong absorbers, and the absorbers from Zabl et al. (2019). The two panels correspond to two different impact parameters which allows a comparison between absorbers nearer to a galaxy and farther from a galaxy. In the left panel, showing stacked spectra at small impact parameters, there is a very clear kinematic picture. The strong absorber spectrum from TNG50 is symmetric and centered at $\sim V_{\text{vir}}/2$, as is the spectrum of Zabl et al. (2019). Thus, qualitatively, strong MgII absorbers as a population generally have LOS velocities in the same direction as their corresponding galaxies' rotations. One slight difference with the stacked spectra for strong absorbers is that the TNG50 spectrum (red line) is somewhat shallower than the observed spectrum (green line). NB:as expected by the factor of ≈ 2 difference in equivalent width at that impact parameter. NB:?! dont understand this?: The lack of dependence on the azimuthal angle α near the major axis on MgII properties found in Figure 4 is present in the kinematics as well.

In Figure 6(left), the only difference between the full fiducial spectrum and the strong absorber-only spectrum is the depth, indicating that, as a population, strong absorbers are not kinematically distinct from absorbers in general at this impact parameter. The precise reason for the discrepancy in the depth is difficult to determine, but it may be sensitive to certain parameters in the TNG physics model (e.g. metal-loading of outflows from supernovae). However, it could also be an effect of simulation resolution (see Section 3.3). So, while TNG50 potentially slightly underproduces the observed amount of MgII gas at 20 kpc, it does possess average kinematics that are consistent with observations at the same region of the CGM.

Figure 6(right) compares the stacked spectra at a larger impact parameter, at $b = 40 \text{ kpc}$. The strong absorbers from TNG50 and MEGAFLOW (Zabl et al. 2019) are both shallower, wider, no longer symmetric, and significantly noisier, though both are still approximately centered around $V_{\text{vir}}/2$. At this impact parameter, the depths of the simulated strong absorber and observed spectra are consistent with each other. However, strong absorbers no longer kinematically resemble the full fiducial sample: in addition to being much rarer at 40 kpc than at 20 kpc, the strong absorbers have larger positive velocities, indicating that MgII in this region is tracing atypically faster moving gas. As was the case at 20 kpc, the difference in the spectra between

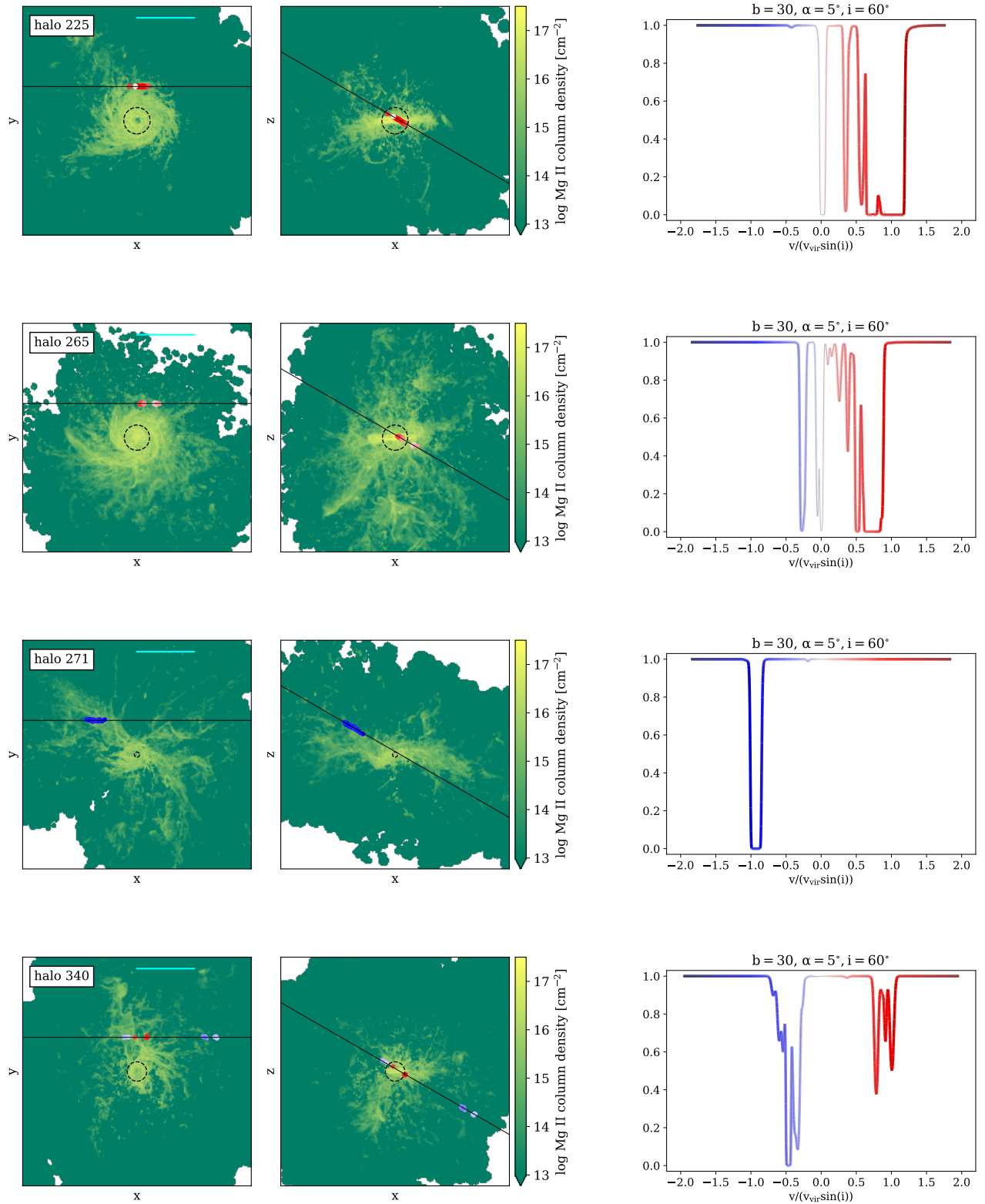


Figure 5. Each row contains two MgII column density maps of a halo from Figure 3 projected along the vertical (left) and horizontal (middle) axis. A sightline at $b = 30$ kpc, $\alpha = 5^\circ$, and $i = 60^\circ$ is overlaid along with gas cells that intersect that sightline and have a MgII column density of at least 10^{12} cm^{-2} , which accounts for $> 95\%$ of the MgII mass along those sightlines. The MgII gas cells and the resulting velocity spectrum (right) are colored by the velocity along the line of sight normalized by $V_{\text{vir}} \sin(i)$, where V_{vir} is the virial velocity of the halo. Dashed circles show twice each galaxy's stellar half-mass radius.

the two azimuth angles is minor. We also note here, but do not show, that the shapes and depths of individual spectra from [Zabl et al. \(2019\)](#) match quite well with particular individual spectra from the much larger fiducial sample from TNG50 (examples of individual spectra from TNG50 are shown in [Figure 5](#)).

3.2. 3D Kinematics of MgII in TNG50

In this section, we characterize the three-dimensional kinematics of the MgII gas in TNG50 and its relation to the observed quantities we discussed in [Section 3.1](#). We show average velocity profiles of the halos in the fiducial sample in [Figure 7](#). The top panel shows the azimuthal velocity component (v_ϕ) in spherical coordinates as a function of radius. We divide gas into cold and hot components based on a temperature threshold of 3×10^4 K, which is chosen to separate the cold and hot clusters seen in the [Figure 2](#), although the profiles are not sensitive to the precise choice of temperature threshold. To understand the relationship of the hot and cold gas to MgII-bearing material we also show the MgII mass-weighted profiles.

First, we see that the MgII gas and the cold gas have nearly identical v_ϕ profiles throughout the halo. In the innermost regions of the CGM, the cold gas has an azimuthal velocity of $\approx 0.6V_{\text{vir}}$ which decreases to $\approx 0.2V_{\text{vir}}$ in the outermost region. Furthermore, though not explicitly shown, most of the cold and MgII gas mass is closer to the major rather than the minor axis because the all- α profiles are much more similar to the $\alpha < 45^\circ$ profiles than the $\alpha > 45^\circ$ profiles. Hot gas has lower azimuthal velocities at all radii and a slightly shallower slope to its profile, but is otherwise qualitatively similar to the cold and MgII gas. This relationship between hot and cold gas is consistent with similar measurements of v_ϕ made from TNG100 in [DeFelippis et al. \(2020\)](#).

In the radial velocity profiles [NB:Which figure?](#), we see a gulf between the velocities of the hot and cold gas develop within ~ 80 kpc where the overall averaged velocity of the gas indicates an inflow at $\sim 0.2V_{\text{vir}}$. Moving towards smaller radii, the cold gas inflow velocities become larger, while hot gas inflow velocities decrease and then switch to **a net** outflow within ~ 40 kpc. The MgII gas still traces the cold gas and reaches typical inflowing velocities of ~ 50 km/s around 30 kpc. However, in the outermost regions of the halo, the radial velocities of all components of the gas converge. The geometry of accretion and outflows is evident from this panel as well: hot gas has especially large **mean** outflowing velocities for $\alpha > 45^\circ$ while cold gas **in the same region has a mean inflowing velocity in the inner halo and nearly no net radial motion in the outer halo.**

Most of the cold and MgII gas mass is moving towards the galaxy in regions surrounding the major axis out to a substantial fraction of the virial radius. It is also clear that kinematically, MgII gas in TNG50 is nearly identical to a simple cut on temperature and so is an excellent tracer of the kinematics of cold CGM gas. In the context of [Section 3.1](#), these results indicate that mock MgII spectra are representative of the entire cold phase of the CGM along the same sightlines.

Finally, we examine the 3D velocities of the MgII gas along our sightlines. In [Figure 8](#) ([see note in caption](#)), we plot stacked spectra for MgII using the three spherical velocity components individually (r , θ , and ϕ), and compare those to the spectrum generated with the full velocity of our fiducial sample of halos. Both the r and θ component spectra are centered at 0 km s^{-1} , indicating that over the entire sample they do not contribute any net velocity shift to the gas along the sightlines. The spectrum of the ϕ component is remarkably similar to the spectrum of the entire velocity, both in terms of velocity shift and width. This means that for our fiducial sample, the shape of the velocity spectra along sightlines is completely determined by only the ϕ (**i.e. rotational**) component of the velocity along those sightlines.

3.3. Effects of halo mass and resolution on MgII in TNG50

We now describe how our main results vary with halo mass and mass resolution. To study the effect of halo mass, we consider two mass bins containing halos from TNG50 with $10^{11} M_\odot < M_{\text{halo}} < 10^{11.5} M_\odot$ and $10^{12} M_\odot < M_{\text{halo}} < 10^{12.5} M_\odot$ at $z = 1$, which are above and below the fiducial mass range and contain 1130 and 167 halos respectively. As in [Section 3.1](#) we calculate MgII equivalent widths and generate velocity spectra which we show in [Figure 9](#). For easier comparison, we also show the TNG50 fiducial sample.

As shown in the left panel of [Figure 9](#), at a given impact parameter, the shape of the equivalent width distribution changes with halo mass: lower halo masses are much more likely to host weak or non-absorbers than higher halo masses, and they are much less likely to host strong absorbers. We find this trend to hold at all impact parameters studied in this paper. We can see the effect on observability with the vertical lines in this panel, which show the mean equivalent widths of the strong absorbers in each mass bin. Typical strong absorbers in the fiducial bin have only slightly larger equivalent widths than those those at lower halo masses, but are substantially weaker than the strong absorbers at higher halo masses. At larger impact parameters, the mean equivalent widths of all strong absorbers is $\approx 0.8 \text{ \AA}$

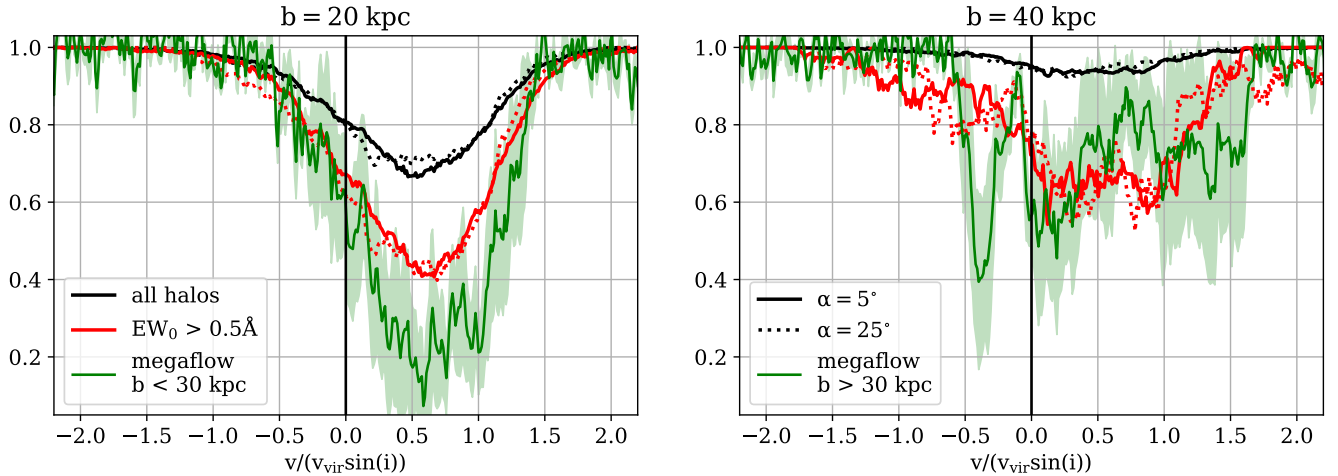


Figure 6. The stacked MgII velocity spectra for the full fiducial TNG50 sample (black) and the subset of strong absorbers (red) for sightlines with $\alpha = 5^\circ$ (solid) and 25° (dotted), and $b = 20$ kpc (left) and 40 kpc (right). Spectra are normalized by $V_{\text{vir}} \sin(i)$, where V_{vir} is the halo’s virial velocity. The green line in each panel is the stacked spectrum of the 4 smallest (left) and largest (right) impact parameters from [Zabl et al. \(2019\)](#), and the green shaded region is an estimate of the error from bootstrapping.

but they are exceedingly rare in lower mass halos. Thus, the primary effects of increasing halo mass on strong absorbers are to increase their occurrence at all impact parameters, especially at large distances, and to increase the mean equivalent width of strong absorbers for halo masses $\gtrsim 10^{12} M_\odot$.

Also shown in the left panel of Figure 9 is the equivalent width distribution of 4315 halos with the same mass as the fiducial bin from the TNG100 simulation, which has a lower baryonic mass resolution than TNG50 by a factor of ~ 16 . Decreasing the simulation resolution lowers equivalent widths overall and steepens the distribution in the same way as decreasing the halo mass does, but the effect is weaker. The mean equivalent width of strong absorbers is largely unaffected by the change in resolution.

In the right panel of Figure 9 we examine the effect of halo mass and resolution on the observed MgII spectrum of strong absorbers. We note that the spectra of the entire samples, as in Figure 6, have the same shape and center as their corresponding strong absorber subset, but are substantially shallower. We also plot the real velocity rather than the normalized velocity to emphasize the difference in equivalent widths, which can be more easily read off.

We see that the fiducial and lower-mass bins have remarkably similar spectra: they are both symmetric and centered at moderate positive velocities. The spectrum of the higher-mass bin is markedly different: it is much broader, asymmetric, and centered at a significantly higher velocity. It still, however, shows a pref-

erence for MgII gas to be corotating. We note that the only difference between Figure 9 as shown and the corresponding normalized spectra is that the normalized higher-mass spectrum is compressed slightly and therefore appears more similar to the normalized fiducial spectrum. Higher halo masses ($\gtrsim 10^{12} M_\odot$) thus have substantially more MgII absorption and more complex kinematic signatures than for the halo masses of the fiducial bin and lower.

Finally, we consider the difference that resolution makes in the MgII absorption spectrum. As was the case with equivalent widths, the difference caused by resolution is smaller than the difference caused by either increasing or decreasing the halo mass. Apart from a slight change in the depth of the spectrum, the kinematic properties of strong absorbers in TNG are essentially resolution independent (**see solid vs. dotted curves in 9 for TNG50 and TNG100 respectively**). The effect of increasing the resolution of the simulation is therefore primarily to increase the occurrence of strong absorbers at a given halo mass.

4. DISCUSSION

4.1. The Role of MgII in TNG

We consider here the ramifications of the detailed analysis of MgII in TNG from Section 3. In Figure 7, we found that MgII gas is very well approximated by a simple temperature cut. Therefore, we expect the angular momentum of cold gas in the CGM of TNG galaxies should be very similar to that of MgII. [DeFelippis et al. \(2020\)](#) found cold CGM gas in halos of this mass range

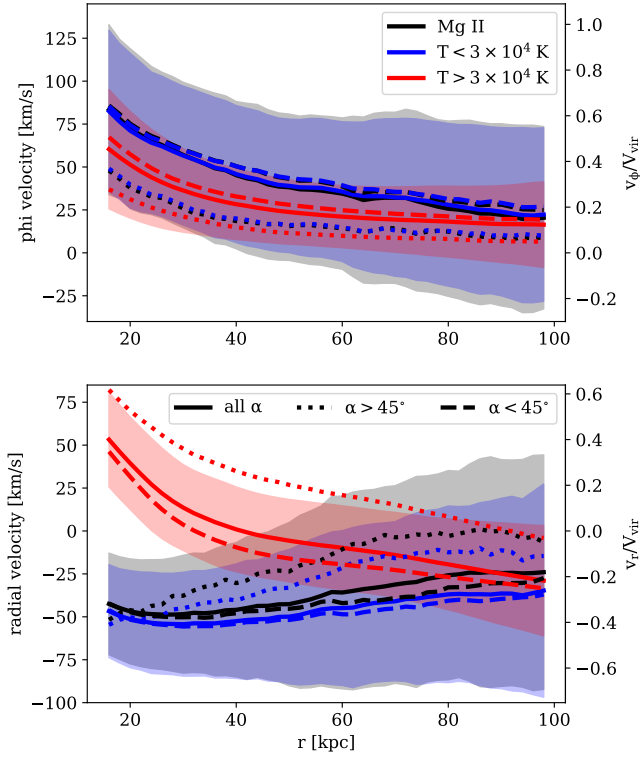


Figure 7. Mean mass-weighted velocity profiles of the spherical phi-component (v_ϕ , top) and r-component (v_r , bottom) of for cold gas (blue), hot gas (red) and MgII gas (black) in spherical bins. Velocity is given in km s^{-1} and as a fraction of the virial velocity. A temperature of 3×10^4 K is used to separate “cold” and “hot” gas. Profiles are shown for gas in the entire halo (solid), gas with $\alpha > 45^\circ$ (dotted), and gas with $\alpha < 45^\circ$ (dashed). Shaded regions show the $\pm 1\sigma$ -scatter of the solid lines and are of similar size for all profiles.

and redshift to have higher angular momentum when surrounding high-angular momentum galaxies, meaning MgII is likely tracing high-angular momentum gas in the CGM of these halos. As the velocity spectrum’s center and shape is almost completely set by the rotational velocity component, it should therefore be possible to use MgII velocity spectra from sightlines near the major axis to estimate the angular momentum of cold gas in the CGM.

In Section 3.3 we examined possible halo mass and resolution dependencies of our results with two main goals in mind: to establish any broad effects of the TNG feedback model on MgII, and to determine to what extent the cosmological simulation can capture MgII kinematics. The results of the halo mass analysis suggest that AGN feedback, which is more dominant at larger halo masses, broadens the velocity and equivalent width dis-

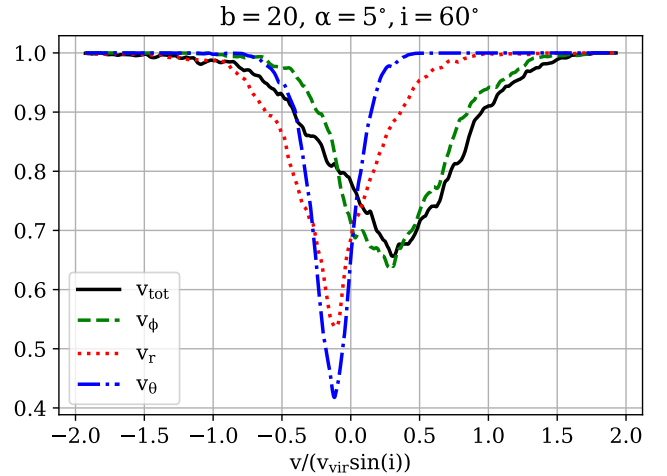


Figure 8. Stacked MgII velocity spectra for the full fiducial TNG50 sample at a single sightline. The contributions of the three spherical components of velocity – v_r (dotted red), v_ϕ (dashed green) and v_θ (dot-dashed blue) – are shown, as well as the spectrum created from the total velocity (solid black). (NOTE: a velocity shift needs to be applied to this figure which will shift all spectra to the right. This will be fixed later.)

tributions and increases the mean absorption at a given impact parameter. For halos with masses $\lesssim 10^{12} M_\odot$, however, kinematic signatures of MgII do not show any significant mass dependence. This is presumably because stellar feedback is the dominant form that affects the CGM for all halo masses below $\sim 10^{12} M_\odot$.

Nelson et al. (2020) has recently used TNG50 to study the origin of cold MgII gas in the CGM of very massive ($M_* \gtrsim 10^{11} M_\odot$) galaxies and found structures of size a few $\times 10^2$ pc that are sufficient to explain the observed covering fractions and line-of-sight kinematics. However, they also note that fundamental properties like the number of cold gas clouds present in halos is not converged even at the resolution of TNG50. Our kinematic results, though, do not qualitatively change even going from TNG50 to TNG100, a factor of ~ 16 in mass resolution. We expect higher resolution simulations to produce more strong absorbers at a given halo mass but the rotation of MgII near the major axis appears to be a resolution-independent aspect of the CGM MEGAFLOW analogs in the TNG simulations.

NB: We need to label the components somehow (dashed/solid and colored lines). Finally, in Figure 10, we show the specific angular momentum (j) of different halo components as a function of stellar mass of their central galaxies, with the goal of contextualizing the angular momentum

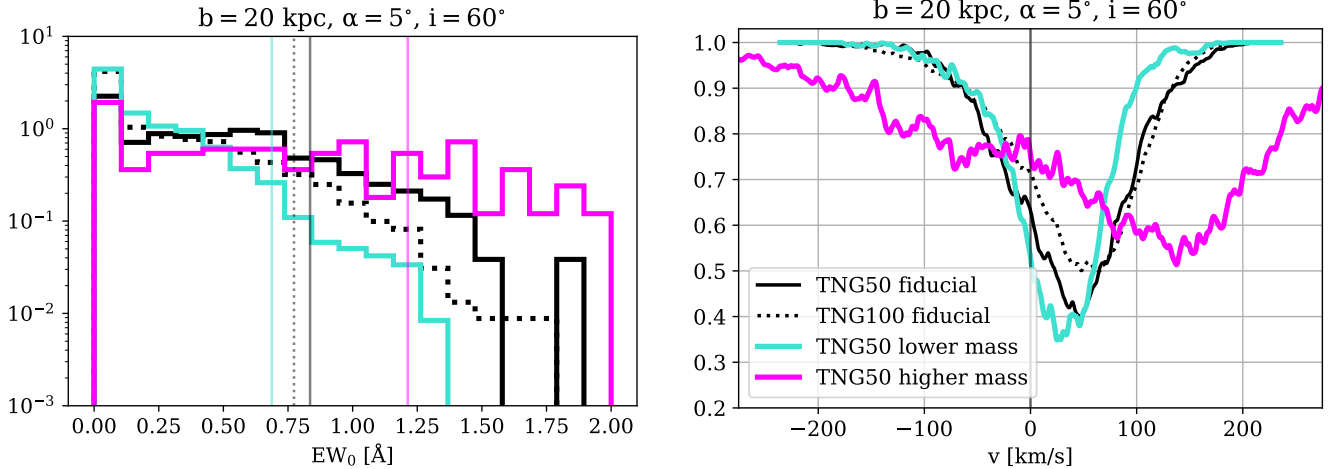


Figure 9. Left: rest-frame equivalent width distribution of the TNG50 fiducial sample (solid black), lower-mass halos with $10^{11} M_{\odot} < M_{\text{halo}} < 10^{11.5} M_{\odot}$ (cyan), higher-mass halos with $10^{12} M_{\odot} < M_{\text{halo}} < 10^{12.5} M_{\odot}$ (magenta) and the same mass halos from TNG100 (dotted black) at the same sightline of $b = 20$ kpc, $\alpha = 5^{\circ}$, and $i = 60^{\circ}$. The mean EW_0 of the strong absorbers in each bin is shown with a translucent vertical line of the same color. Right: Stacked velocity spectra of the same halo samples with velocities in km s^{-1} .

of MgII gas in relation to the rest of the gas in the CGM as well as to the other components of the halo. The slope of this $j - M_*$ relation for the stellar component of galaxies is ~ 0.6 as generally observed (Fall & Romanowsky 2013, e.g.), and all other components appear to have roughly identical slopes. Most interesting are the relative positions of the CGM and dark matter on this plane. At a given stellar mass, all components of the CGM have a slightly higher typical j than that of the dark matter. There are multiple potential reasons for this. First, galaxies can remove low-angular momentum gas from the CGM by either accreting it and using it to form stars. Feedback from stars and/or AGN can also eject low-angular momentum gas from the halo completely. Finally, dark matter in the halo can transfer some of its angular momentum to the gas. Regardless, it is clear that MgII traces the angular momentum of the CGM quite well. NB:Do we need this?:, though not as well as rotational velocities (Figure 7) presumably due to the much more centralized mass distribution of the MgII compared to all of the gas in the CGM.

4.2. Comparisons to Recent Work

We now highlight results from previous work on MgII absorption in observations and simulations in the context of our results. Observations of MgII using sightlines near the major axis of galaxies have generally found that gas is corotating with the galaxy both for small impact

parameters of < 15 kpc (Bouché et al. 2016, e.g.) and large impact parameters of > 50 kpc (e.g. Martin et al. 2019). Using a lensed system, Lopez et al. (2020) observed multiple sightlines of the same CGM and measured a decreasing MgII rotation curve that is qualitatively similar to Figure 7. However, their absorption data only goes out to ≈ 30 kpc. Our work suggests MgII rotation curves should continue to decrease to at least 100 kpc, though based on the maps in Figure 3 the MgII column densities at those distances are significantly below current observational limits.

While this paper is focused on MgII gas near the major axis, there are also recent results suggesting MgII outflows along the minor axis of galaxies with velocities $> 100 \text{ km s}^{-1}$ (e.g. Schroetter et al. 2019; Zabl et al. 2020). It is worth noting though that Mortensen et al. (2020) found a lensed system with MgII on the geometric minor axis of the absorber galaxy with line-of-sight velocities $< 100 \text{ km s}^{-1}$ and a large velocity dispersion, indicating that the kinematics of MgII outflows may vary significantly. Importantly, the TNG fiducial sample does not display large radial velocities for MgII gas in regions of the CGM around the minor axis, and it is only gas that is higher than typical temperatures of MgII gas that has any average outflows which are still $< 100 \text{ km s}^{-1}$. Therefore, while the fiducial sample from TNG replicates the observed rotational aspect of MgII gas, it does not produce cold outflows that are inferred from observations at $z \approx 1$.

Ho et al. (2020) recently studied similar aspects of MgII absorption in the EAGLE simulation at $z \approx 0.3$

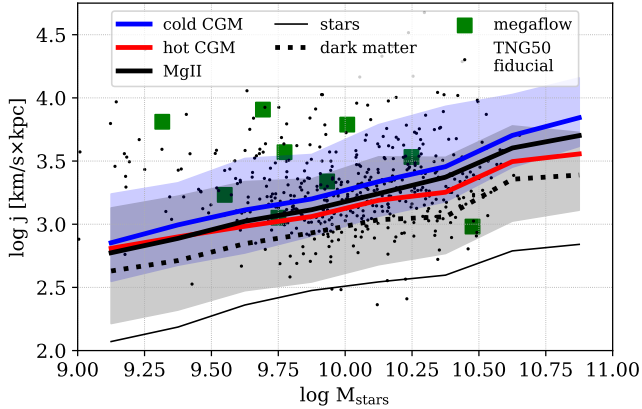


Figure 10. Median specific angular momentum vs galactic stellar mass for the cold (blue), hot (red), and MgII (thick black) CGM as defined in Figure 7, as well as the dark matter halo (dotted black) and the stellar component of the galaxy (thin black) at $z = 1$. Unlike previous figures, medians are calculated using a sample of all halos with galaxies that have $10^9 M_{\odot} < M_* < 10^{11} M_{\odot}$. Shaded regions show the 16th and 84th percentiles of the distributions of the cold gas (blue), which is similar in size to all components except dark matter (black) which has noticeably larger scatter. Black points show the MgII specific angular momentum of the halo mass-selected TNG50 fiducial sample which is biased towards higher j for $M_* \lesssim 10^{9.75}$. Green squares show estimations for the specific angular momentum of the MEGAFLOW absorbers using inferred rotational velocities from Zabl et al. (2019).

and found results broadly consistent with ours. Specifically, they measure a rotating MgII structure around star-forming galaxies as well as a lower detection fraction of MgII near the minor axis. They also find that higher-mass galaxies host detectable (i.e. above a fixed column density) MgII structures out to larger distances in the CGM, which we indirectly show with the EW distributions in Figure 9, where higher-mass halos have more strong absorbers.

5. SUMMARY

We have simulated MgII absorption in the CGM of halos from TNG50 comparable to those observed in the MEGAFLOW sample and compared absorption and kinematic properties of the two samples. We also examined the 3D kinematics of the MgII in TNG50. Our conclusions are as follows:

1. The equivalent widths of absorber-selected halos (i.e. strong absorbers) from TNG50 match reasonably well with the equivalent widths of major-axis sightlines

from MEGAFLOW (Zabl et al. 2019). **NB: Do you think this is a significant result?;, but the simulated halos appear to underproduce MgII absorption at smaller impact parameters.**

2. A majority of halos are strong absorbers at the smallest impact parameter studied (15 kpc), but the strong absorber fraction drops quickly as a function of distance.
3. The stacked velocity spectra of TNG50 strong absorbers match the stack spectra of Zabl et al. (2019) very well, **thus supporting the physical interpretation of co-rotation** both below 30 kpc, where the spectra are strongly peaked near $\sim 0.5V_{\text{vir}}$ and symmetric, and above 30 kpc, where the spectra are similarly peaked but are much noisier, broader, and asymmetric.
4. In TNG, MgII gas has velocity profiles nearly identical to gas below a temperature cutoff of 3×10^4 K, **meaning MgII absorption is a good proxy for cold gas kinematics in general.** There is substantial rotation and typical inflow velocities of $\sim 50 \text{ km s}^{-1}$ out to ~ 60 kpc in the CGM.
5. The radial and polar velocity components by themselves do not cause any net velocity shift in the spectrum, **which implies that MgII absorption kinematics alone cannot be used to measure inflows of systems with edge-on geometries.**
6. MgII absorption strengths and spectra are stronger and broader for halos more massive than the fiducial sample **of $10^{11.5} - 10^{12} M_{\odot}$ halos** but do not change very much for halos less massive than the fiducial sample. Lowering the resolution from TNG50 to TNG100 only modestly changes any of the MgII kinematic properties.
7. Our results from TNG50 are consistent with the emerging picture of rotating MgII gas found in observations and other simulations, but there seems to be a lack of MgII outflows along the minor axes.

This work demonstrates that generating mock MgII observations from TNG50 generates absorption spectra that are comparable to real data. In future work, we plan to widen our investigation to include other ions that trace warmer and more diffuse gas, as well as follow gas at particular redshifts backwards and forwards through time to determine the stability of various ion structures and their role in transporting angular momentum to or from the galaxy.

ACKNOWLEDGMENTS

We thank Johannes Zabl, Edouard Tollet, Joakim Rosdahl and Jeremy Blaizot for insightful and useful discussions, as well as Cameron Hummels for assistance with TRIDENT. **D.D. acknowledges support from the Chateaubriand Fellowship of the Office for Science Technology of the Embassy of France in the United States.** Flatiron Institute is supported by the Simons Foundation. GLB acknowledges financial support from the NSF (grant AST-1615955, OAC-1835509) and computing support from NSF XSEDE. **F.M. acknowledges support through the Program Rita Levi Montalcini of the Italian MUR.** **N.B acknowledges funding support from the French Agence National de Recherche (ANR) grant ‘3DGasFlows’ (ANR-17-CE31-0017).**

Software: TRIDENT (Hummels et al. 2017), YT (Turk et al. 2011), CLOUDY (Ferland et al. 2013), NUMPY (van

der Walt et al. 2011), MATPLOTLIB (Hunter 2007), and IPYTHON (Perez & Granger 2007)

REFERENCES

- Bacon, R., Bauer, S., Boehm, P., et al. 2006, in Society of Photo-Optical Instrumentation Engineers (SPIE) Conference Series, Vol. 6269, Society of Photo-Optical Instrumentation Engineers (SPIE) Conference Series, ed. I. S. McLean & M. Iye, 62690J, doi: [10.1117/12.669772](https://doi.org/10.1117/12.669772)
- Bergeron, J., & Boissé, P. 1991, A&A, 243, 344
- Bergeron, J., Cristiani, S., & Shaver, P. A. 1992, A&A, 257, 417
- Bordoloi, R., Lilly, S. J., Knobel, C., et al. 2011, ApJ, 743, 10, doi: [10.1088/0004-637X/743/1/10](https://doi.org/10.1088/0004-637X/743/1/10)
- Bouché, N., Hohensee, W., Vargas, R., et al. 2012, MNRAS, 426, 801, doi: [10.1111/j.1365-2966.2012.21114.x](https://doi.org/10.1111/j.1365-2966.2012.21114.x)
- Bouché, N., Murphy, M. T., Kacprzak, G. G., et al. 2013, Science, 341, 50, doi: [10.1126/science.1234209](https://doi.org/10.1126/science.1234209)
- Bouché, N., Finley, H., Schroetter, I., et al. 2016, ApJ, 820, 121, doi: [10.3847/0004-637X/820/2/121](https://doi.org/10.3847/0004-637X/820/2/121)
- Bryan, G. L., & Norman, M. L. 1998, ApJ, 495, 80, doi: [10.1086/305262](https://doi.org/10.1086/305262)
- Burchett, J. N., Rubin, K. H. R., Prochaska, J. X., et al. 2020, arXiv e-prints, arXiv:2005.03017. <https://arxiv.org/abs/2005.03017>
- Burchett, J. N., Tripp, T. M., Prochaska, J. X., et al. 2019, ApJL, 877, L20, doi: [10.3847/2041-8213/ab1f7f](https://doi.org/10.3847/2041-8213/ab1f7f)
- Coil, A. L., Blanton, M. R., Burles, S. M., et al. 2011, ApJ, 741, 8, doi: [10.1088/0004-637X/741/1/8](https://doi.org/10.1088/0004-637X/741/1/8)
- Corlies, L., Peebles, M. S., Tumlinson, J., et al. 2020, ApJ, 896, 125, doi: [10.3847/1538-4357/ab9310](https://doi.org/10.3847/1538-4357/ab9310)
- Danovich, M., Dekel, A., Hahn, O., Ceverino, D., & Primack, J. 2015, MNRAS, 449, 2087, doi: [10.1093/mnras/stv270](https://doi.org/10.1093/mnras/stv270)
- DeFelippis, D., Genel, S., Bryan, G. L., & Fall, S. M. 2017, ApJ, 841, 16, doi: [10.3847/1538-4357/aa6dfc](https://doi.org/10.3847/1538-4357/aa6dfc)
- DeFelippis, D., Genel, S., Bryan, G. L., et al. 2020, ApJ, 895, 17, doi: [10.3847/1538-4357/ab8a4a](https://doi.org/10.3847/1538-4357/ab8a4a)
- Dutta, R., Fumagalli, M., Fossati, M., et al. 2020, MNRAS, 499, 5022, doi: [10.1093/mnras/staa3147](https://doi.org/10.1093/mnras/staa3147)
- Fall, S. M., & Romanowsky, A. J. 2013, ApJL, 769, L26, doi: [10.1088/2041-8205/769/2/L26](https://doi.org/10.1088/2041-8205/769/2/L26)
- Faucher-Giguère, C.-A., Lidz, A., Zaldarriaga, M., & Hernquist, L. 2009, ApJ, 703, 1416, doi: [10.1088/0004-637X/703/2/1416](https://doi.org/10.1088/0004-637X/703/2/1416)
- Ferland, G. J., Porter, R. L., van Hoof, P. A. M., et al. 2013, RMxAA, 49, 137. <https://arxiv.org/abs/1302.4485>
- Ho, S. H., Martin, C. L., Kacprzak, G. G., & Churchill, C. W. 2017, ApJ, 835, 267, doi: [10.3847/1538-4357/835/2/267](https://doi.org/10.3847/1538-4357/835/2/267)
- Ho, S. H., Martin, C. L., & Schaye, J. 2020, ApJ, 904, 76, doi: [10.3847/1538-4357/abbe88](https://doi.org/10.3847/1538-4357/abbe88)
- Ho, S. H., Martin, C. L., & Turner, M. L. 2019, ApJ, 875, 54, doi: [10.3847/1538-4357/ab0ec2](https://doi.org/10.3847/1538-4357/ab0ec2)
- Hummels, C. B., Smith, B. D., & Silvia, D. W. 2017, ApJ, 847, 59, doi: [10.3847/1538-4357/aa7e2d](https://doi.org/10.3847/1538-4357/aa7e2d)
- Hummels, C. B., Smith, B. D., Hopkins, P. F., et al. 2019, ApJ, 882, 156, doi: [10.3847/1538-4357/ab378f](https://doi.org/10.3847/1538-4357/ab378f)

- Hunter, J. D. 2007, *Computing in Science Engineering*, 9, 90, doi: [10.1109/MCSE.2007.55](https://doi.org/10.1109/MCSE.2007.55)
- Lan, T.-W. 2020, *ApJ*, 897, 97, doi: [10.3847/1538-4357/ab989a](https://doi.org/10.3847/1538-4357/ab989a)
- Lan, T.-W., & Mo, H. 2018, *ApJ*, 866, 36, doi: [10.3847/1538-4357/aadc08](https://doi.org/10.3847/1538-4357/aadc08)
- Lopez, S., Tejos, N., Barrientos, L. F., et al. 2020, *MNRAS*, 491, 4442, doi: [10.1093/mnras/stz3183](https://doi.org/10.1093/mnras/stz3183)
- Marinacci, F., Vogelsberger, M., Pakmor, R., et al. 2018, *MNRAS*, 480, 5113, doi: [10.1093/mnras/sty2206](https://doi.org/10.1093/mnras/sty2206)
- Martin, C. L., Ho, S. H., Kacprzak, G. G., & Churchill, C. W. 2019, *ApJ*, 878, 84, doi: [10.3847/1538-4357/ab18ac](https://doi.org/10.3847/1538-4357/ab18ac)
- Mortensen, K., Keerthi Vasan G., C., Jones, T., et al. 2020, arXiv e-prints, arXiv:2006.00006. <https://arxiv.org/abs/2006.00006>
- Naiman, J. P., Pillepich, A., Springel, V., et al. 2018, *MNRAS*, 477, 1206, doi: [10.1093/mnras/sty618](https://doi.org/10.1093/mnras/sty618)
- Nelson, D., Pillepich, A., Springel, V., et al. 2018, *MNRAS*, 475, 624, doi: [10.1093/mnras/stx3040](https://doi.org/10.1093/mnras/stx3040)
- . 2019, *MNRAS*, 490, 3234, doi: [10.1093/mnras/stz2306](https://doi.org/10.1093/mnras/stz2306)
- Nelson, D., Sharma, P., Pillepich, A., et al. 2020, arXiv e-prints, arXiv:2005.09654. <https://arxiv.org/abs/2005.09654>
- Nielsen, N. M., Churchill, C. W., Kacprzak, G. G., & Murphy, M. T. 2013, *ApJ*, 776, 114, doi: [10.1088/0004-637X/776/2/114](https://doi.org/10.1088/0004-637X/776/2/114)
- Nielsen, N. M., Churchill, C. W., Kacprzak, G. G., Murphy, M. T., & Evans, J. L. 2015, *ApJ*, 812, 83, doi: [10.1088/0004-637X/812/1/83](https://doi.org/10.1088/0004-637X/812/1/83)
- Peeples, M. S., Corlies, L., Tumlinson, J., et al. 2019, *ApJ*, 873, 129, doi: [10.3847/1538-4357/ab0654](https://doi.org/10.3847/1538-4357/ab0654)
- Perez, F., & Granger, B. E. 2007, *Computing in Science Engineering*, 9, 21, doi: [10.1109/MCSE.2007.53](https://doi.org/10.1109/MCSE.2007.53)
- Pillepich, A., Nelson, D., Hernquist, L., et al. 2018, *MNRAS*, 475, 648, doi: [10.1093/mnras/stx3112](https://doi.org/10.1093/mnras/stx3112)
- Pillepich, A., Nelson, D., Springel, V., et al. 2019, *MNRAS*, 490, 3196, doi: [10.1093/mnras/stz2338](https://doi.org/10.1093/mnras/stz2338)
- Putman, M. E. 2017, *Astrophysics and Space Science Library*, Vol. 430, *An Introduction to Gas Accretion onto Galaxies*, ed. A. Fox & R. Davé, 1, doi: [10.1007/978-3-319-52512-9_1](https://doi.org/10.1007/978-3-319-52512-9_1)
- Ramos Padilla, A. F., Wang, L., Ploekinger, S., van der Tak, F. F. S., & Trager, S. 2020, arXiv e-prints, arXiv:2011.13441. <https://arxiv.org/abs/2011.13441>
- Rickards Vaught, R. J., Rubin, K. H. R., Arrigoni Battaia, F., Prochaska, J. X., & Hennawi, J. F. 2019, *ApJ*, 879, 7, doi: [10.3847/1538-4357/ab211f](https://doi.org/10.3847/1538-4357/ab211f)
- Rubin, K. H. R., Diamond-Stanic, A. M., Coil, A. L., Crighton, N. H. M., & Stewart, K. R. 2018, *ApJ*, 868, 142, doi: [10.3847/1538-4357/aad566](https://doi.org/10.3847/1538-4357/aad566)
- Rubin, K. H. R., Prochaska, J. X., Ménard, B., et al. 2011, *ApJ*, 728, 55, doi: [10.1088/0004-637X/728/1/55](https://doi.org/10.1088/0004-637X/728/1/55)
- Rudie, G. C., Steidel, C. C., Trainor, R. F., et al. 2012, *ApJ*, 750, 67, doi: [10.1088/0004-637X/750/1/67](https://doi.org/10.1088/0004-637X/750/1/67)
- Rupke, D. S. N., Coil, A., Geach, J. E., et al. 2019, *Nature*, 574, 643, doi: [10.1038/s41586-019-1686-1](https://doi.org/10.1038/s41586-019-1686-1)
- Schroetter, I., Bouché, N., Wendt, M., et al. 2016, *ApJ*, 833, 39, doi: [10.3847/1538-4357/833/1/39](https://doi.org/10.3847/1538-4357/833/1/39)
- Schroetter, I., Bouché, N. F., Zabl, J., et al. 2019, *MNRAS*, 490, 4368, doi: [10.1093/mnras/stz2822](https://doi.org/10.1093/mnras/stz2822)
- . 2021, *MNRAS*, submitted (astro-ph/2012.04935)
- Springel, V. 2010, *MNRAS*, 401, 791, doi: [10.1111/j.1365-2966.2009.15715.x](https://doi.org/10.1111/j.1365-2966.2009.15715.x)
- Springel, V., & Hernquist, L. 2003, *MNRAS*, 339, 289, doi: [10.1046/j.1365-8711.2003.06206.x](https://doi.org/10.1046/j.1365-8711.2003.06206.x)
- Springel, V., Pakmor, R., Pillepich, A., et al. 2018, *MNRAS*, 475, 676, doi: [10.1093/mnras/stx3304](https://doi.org/10.1093/mnras/stx3304)
- Steidel, C. C., & Sargent, W. L. W. 1992, *ApJS*, 80, 1, doi: [10.1086/191660](https://doi.org/10.1086/191660)
- Stewart, K. R., Brooks, A. M., Bullock, J. S., et al. 2013, *ApJ*, 769, 74, doi: [10.1088/0004-637X/769/1/74](https://doi.org/10.1088/0004-637X/769/1/74)
- Stewart, K. R., Kaufmann, T., Bullock, J. S., et al. 2011, *ApJ*, 738, 39, doi: [10.1088/0004-637X/738/1/39](https://doi.org/10.1088/0004-637X/738/1/39)
- Stewart, K. R., Maller, A. H., Oñorbe, J., et al. 2017, *ApJ*, 843, 47, doi: [10.3847/1538-4357/aa6dff](https://doi.org/10.3847/1538-4357/aa6dff)
- Suresh, J., Nelson, D., Genel, S., Rubin, K. H. R., & Hernquist, L. 2019, *MNRAS*, 483, 4040, doi: [10.1093/mnras/sty3402](https://doi.org/10.1093/mnras/sty3402)
- Tumlinson, J., Peeples, M. S., & Werk, J. K. 2017, *ARA&A*, 55, 389, doi: [10.1146/annurev-astro-091916-055240](https://doi.org/10.1146/annurev-astro-091916-055240)
- Tumlinson, J., Thom, C., Werk, J. K., et al. 2011, *Science*, 334, 948, doi: [10.1126/science.1209840](https://doi.org/10.1126/science.1209840)
- Turk, M. J., Smith, B. D., Oishi, J. S., et al. 2011, *ApJS*, 192, 9, doi: [10.1088/0067-0049/192/1/9](https://doi.org/10.1088/0067-0049/192/1/9)
- Turner, M. L., Schaye, J., Steidel, C. C., Rudie, G. C., & Strom, A. L. 2014, *MNRAS*, 445, 794, doi: [10.1093/mnras/stu1801](https://doi.org/10.1093/mnras/stu1801)
- van der Walt, S., Colbert, S. C., & Varoquaux, G. 2011, *Computing in Science Engineering*, 13, 22, doi: [10.1109/MCSE.2011.37](https://doi.org/10.1109/MCSE.2011.37)
- Weinberger, R., Springel, V., & Pakmor, R. 2019, arXiv e-prints, arXiv:1909.04667. <https://arxiv.org/abs/1909.04667>
- Wendt, M., Bouché, N. F., Zabl, J., Schroetter, I., & Muzahid, S. 2021, *MNRAS*, doi: [10.1093/mnras/stab049](https://doi.org/10.1093/mnras/stab049)
- Werk, J. K., Prochaska, J. X., Thom, C., et al. 2013, *ApJS*, 204, 17, doi: [10.1088/0067-0049/204/2/17](https://doi.org/10.1088/0067-0049/204/2/17)
- Zabl, J., Bouché, N. F., Schroetter, I., et al. 2019, *MNRAS*, 485, 1961, doi: [10.1093/mnras/stz392](https://doi.org/10.1093/mnras/stz392)

—. 2020, MNRAS, 492, 4576, doi: [10.1093/mnras/stz3607](https://doi.org/10.1093/mnras/stz3607)

Zabl, J., Bouché, N. F., Wisotzki, L., et al. 2021, MNRAS, submitted

Zhu, G., & Ménard, B. 2013, ApJ, 770, 130,
doi: [10.1088/0004-637X/770/2/130](https://doi.org/10.1088/0004-637X/770/2/130)